Remote Sensing of Environment 253 (2021) 112152

Contents lists available at ScienceDirect

Remote Sensing of Environment

journal homepage: www.elsevier.com/locate/rse

Joint exploitation of spaceborne SAR images and GIS techniques for urban coherent change detection

Marco Manzoni *, Andrea Monti-Guarnieri, Monia Elisa Molinari

Dipartimento di Elettronica, Informazione e Bioingegneria, Politecnico di Milano, Via Giuseppe Ponzio 34, Milan, Italy

ARTICLE INFO

Keywords:
Change detection
SAR
Urban
GIS
CCD

ABSTRACT

This paper proposes a simple and fast method for the identification of structural changes affecting buildings in urban environments by using a combination of Synthetic Aperture Radar (SAR) imagery and Geospatial Information System (GIS) processing.

The identification of changes in urban settlements is of great interest for damage assessment after natural disasters, cadastral mapping and monitoring urban development or illegal activities, such as the construction of unauthorized buildings.

Satellite remote sensing is useful in this scenario and SAR data is attractive due to its wide and ubiquitous coverage, the day and night all-weather availability, the exact repetition of the acquisition geometry, the repeated illumination and the sensitivity to slight changes in the geometrical structure of the targets in the scene.

This sensibility is an advantage, but turns into a drawback especially in an urban environment where every subtle change may cause an unwanted detection.

This environment is indeed one of the most challenging for the detection of those changes that are of any real interest since these events are masked by thousands of irrelevant detections.

This paper tackle this problem with a combination of an improved, high-resolution coherent change detection technique called M-CCD and with a GIS post-processing. The result is a map of changes affecting buildings that are of a significant scale and consequently of a certain interest in an urban environment.

In this contribution, the complete workflow is detailed and an assessment of the detected changes is done with high resolution optical images through visual photo-interpretation. A comparison with other SAR and optical change detection methods is also carried out.

1. Introduction

The detection of changes is one of the most important applications of Synthetic Aperture Radar interferometry.

The free and open availability of systematic repeated-pass SAR images, made possible with the ESA mission Sentinel-1 starting from 2014, provided a huge boost in the research field concerning change detection (Colin Koeniguer and Nicolas, 2020; Hakdaoui et al., 2019; Luo et al., 2019; Olen and Bookhagen, 2018; Washaya et al., 2018).

The advantages of SAR sensors with respect to optical sensors in this particular field are manifold: the complete immunity to cloud coverage, the possibility to sense the scene even at night, the repeated geometry of acquisition and illumination and, the most important, the high sensitivity to fine changes in the geometrical structure of the scene (Moreira et al., 2013).

The monitoring of urban settlements is a particularly interesting topic in the remote sensing community. Tracking the rapid changing in the urban landscapes and its effect on the environment (Ehrlich et al., 2018), monitoring buildings construction or demolition (Chini et al., 2018; Tamura, 2015) and the generation of land cover land use maps over human settlements (Atwood and Thirion-Lefevre, 2018; Pan et al., 2019) are just three of the multitude of possible applications of remote sensing and change detection over civilized areas (Gamba et al., 2008; Melchiorri et al., 2018; Montuori et al., 2016).

A SAR is a coherent sensing system in which both the amplitude and the phase of the signal backscattered from the targets on the ground are measured. The amplitude is related to the radar reflectivity, like for optical images, while the phase is sensitive to the target's location with the accuracy of the centimeter.

One could choose to use just the first one and search for a change in

* Corresponding author.
E-mail address: marco.manzoni@polimi.it (M. Manzoni).

https://doi.org/10.1016/j.rse.2020.112152
Received 10 April 2020; Received in revised form 24 September 2020; Accepted 20 October 2020
Available online 2 November 2020

the radar reflectivity. This method, while effective for the detection of big changes in the radiometric signature of the targets, is ineffective in the case of subtle changes where the scattered energy remains the same between two acquisitions. The simplicity of radiometric-based methods contributed to the proliferation of the incoherent analysis in literature (Aiazzi et al., 2013; Bovolo and Bruzzone, 2005; Bovolo et al., 2013; Bujor et al., 2004; Marin et al., 2015; Rignot and van Zyl, 1993).

Coherent change detection (CCD), instead, exploits the phase of the backscatter, that is related to the wavelength (5.6 cm in C-band), leading to a much higher sensitivity. Also these techniques, as the incoherent ones, were extensively discussed in the literature (Biondi, 2018; Jung et al., 2016; Mian et al., 2019; Novak, 2005; Perissin and Wang, 2011; Wahl et al., 2016).

The sensibility of the system to small changes is a double-edge blade. A huge number of changes can be triggered due to slight variations that are not of interest: these nuisance detections are numerous, therefore they can hinder the recognition of interesting changes.

Obviously, this problem only becomes worse as the SAR operational frequency increases since the wavelength is reduced and the phase sensitivity is higher.

The detection of unwanted changes is particularly pronounced in turbolent and ever-changing environments like the urban one, where plenty of sources of decorrelation are present from parking lots to green areas and streets. The challenges for a coherent change detection method are not only limited to the space domain (a lot of unwanted detection in different places), but also in time since multiple changes may occur along the total observation period.

In this scenario, assuming a model where only one change happens in the whole time series can be insufficient, therefore, a more robust estimator must be implemented together with a method to suppress all the changes that are not of any interest.

The method here proposed for detecting changes affecting buildings exploits the sensitivity of coherent approaches while reducing at most the number of false alarm basing on the maximization of the change likelihood. This is achieved by:

1. Combining a fine phase calibration to compensate for the effect of elevation;
2. A hierarchical identification of multiple changes occurring over the same target. This method will be called from now on Multiple-Coherent Change Detection (M-CCD);
3. An a-posteriori processing to generate clusters of changes over the same building and provide a proper threshold to detect them.

The method is detailed in Section 2 together with the complete processing chain.

In Section 3, a case study for the city of Manchester (UK) is presented. For the data processing we used several configurations of the proposed estimator each one with different combination of polarization, estimation window and threshold for the detection. Since a ground truth of changes in not available in this scenario, high-resolution optical images have been exploited to provide a first interpretation of the changes.

In Section 4 we provide a comparison with other SAR and optical change detection techniques. In the last section conclusions are drawn.

2. Methodology

In this section the complete workflow is presented starting from the mandatory pre-processing of the data and ending with the GIS-based post-processing. In Fig. 1 the entire scheme is depicted.

2.1. Data pre-processing

SAR images need an ad-hoc pre-processing: this includes amplitude calibration, fine coregistration (at sub-pixel level) (Sansosti et al., 2006), and, in the case of burst-mode acquisitions like for Sentinel-1, a proper debursting (De Zan and Monti Guarnieri, 2006). This is sufficient for incoherent change detection methods.

If coherent processing is needed, also the phase of the images needs to be properly calibrated (Freeman, 1992). Since the phase senses the sensor-target optical path, the following elements have an impact on the measure:

1. The satellite changes position between one acquisition and the other since it is not able to repeat exactly the same orbit (see Fig. 2). This condition generates in the interferometric data a term that is proportional to the local topography.
2. The variation of the optical path due to the different conditions of propagation in the atmosphere.
3. The change in the position of target or in the structure of a part of the many scatterers inside the resolution cell.

The first two terms must be compensated if the final objective is the assessment of the changes. The first one can be removed by using a Digital Elevation Model of the scene while the second by jointly exploiting a stack of images as widely discussed in (Manzoni et al., 2020; Monti-Guarnieri et al., 2018). Note that it is necessary to compensate the

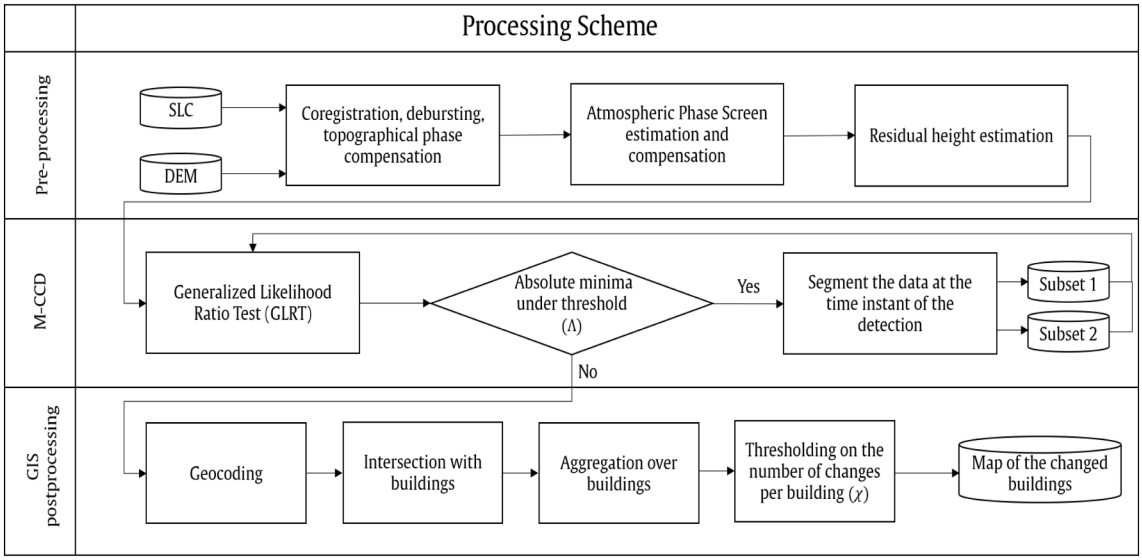

Fig. 1. Processing scheme.

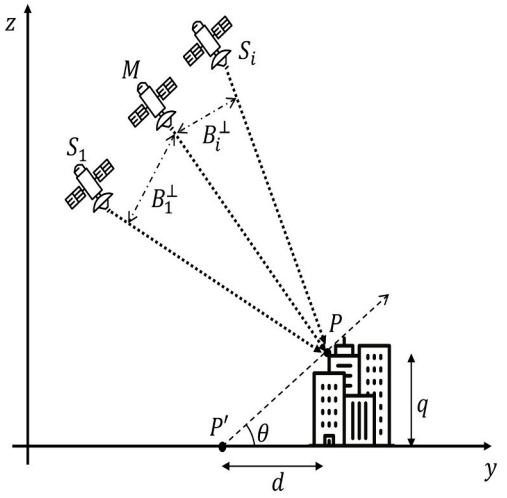

Fig. 2. The acquisition geometry of a multipass SAR. The resolution along the z coordinate is given by the synthetic aperture obtained with multiple passages. The master acquisition is denoted with M while $B_i^{\perp}$ is the normal baseline between the master and the i^{th} slave.

topographic phase up to the limits represented by the knowledge of the exact orbit and the DEM vertical and horizontal resolution. This is the reason why a further step is necessary to estimate and remove the residual topographic component in the interferometric phase.

2.2. Residual height estimation

In an urban environment the compensation of the topographical phase may be inaccurate due to the large discrepancy between the DEM and the real topography of the scene. The presence of a residual term due to the elevation of the target can generate two unwanted effects:

1. False alarms can be triggered by the imperfect compensation of the sensor-target distance due to DEM errors;
2. A geocoding error that locates the target in a wrong geographical position, preventing the proper functioning of the GIS post-processing.

The latter problem can be better explained by looking at Fig. 2: the target at position P will be geolocated at position P' if its elevation q is assumed to be null. The location error on the ground would be $d = q/\tan(\theta)$, which could account for tens of meters in an urban scenario. The solution is to recur to a processing able to extract the residual height q from the data and, in turn, using the local incidence angle θ to find the displacement d to compensate for.

In the following we detail the technique used for the estimation of the residual height and we evaluate the performances of the method. In presence of a single point scatterer in a resolution cell, a pixel of the i^{th} SLC image can be modeled as (Hanssen, 2001):

$$g_i = \rho e^{j\frac{4\pi}{\lambda}\frac{B_i^{\perp}}{R\sin(\theta)}q} = \rho e^{jk_z q} \tag{1}$$

where ρ is the complex reflectivity function entailing both the amplitude and the phase of the backscattered signal, $B_i^{\perp}$ is the normal baseline between the master orbit and the i^{th} slave, θ is the local incidence angle, q is the residual height to estimate, R is the slant range distance between sensor and target, λ is the wavelength and k_z is the so called vertical interferometric wavenumber (or height-to-phase conversion factor).

Since the geometry of the acquisition is known very well thanks to precise orbits available for Sentinel-1 products, the only parameter to estimate in eq. 1 is the residual height. The simplest solution is to explore a set of possible heights by cross-correlating the complex time series of a pixel with the model for the topographic phase.

This operation actually minimizes the L2 norm of the difference between the data and the model:

$$\widehat{q} = arg\,min_q \parallel \mathbf{g} - \mathbf{m}(q)\|_2^2 \sim arg\,max_q \mathbf{g}^H \mathbf{m}(q) \tag{2}$$

where $\mathbf{g} = [g_1\ g_2\ g_3\ \dots\ g_N]^T$ is the complex time series of a single pixel in the scene and

$$\mathbf{m}(q) = \left[e^{-j\frac{4\pi B_1^{\perp}}{\lambda R\sin\theta}q},\ e^{-j\frac{4\pi B_2^{\perp}}{\lambda R\sin\theta}q},\ \dots,\ e^{-j\frac{4\pi B_N^{\perp}}{\lambda R\sin\theta}q} \right]^T \tag{3}$$

is the vector containing all the phase terms due to the residual topography. The mean accuracy in the estimation of the height can be derived by a simple linear model where the unwrapped phases are employed. The model is the following:

$$\phi = \mathbf{K_z} q + \mathbf{w} \tag{4}$$

where ϕ is the $N_i \times 1$ vector containing the time series of the phases of a single pixel in the scene, $\mathbf{K_z}$ is the $N_i \times 1$ vector containing all the phase to height conversion factors as in eq. 1, q is the residual height to be estimated and $\mathbf{w}$ is the $N_i \times 1$ vector representing the noise. The variance on the estimate is easily derived as:

$$\sigma_q^2 = \left(\mathbf{K_z}^T \mathbf{K_z}\right)^{-1} \sigma_w^2 \tag{5}$$

with a $\sigma_w = 1$ rad, an average baseline of 30 m and an average incidence angle of 35 degree we can obtain a standard deviation from eq. 5 of 4 m with as low as 10 images: more than enough for the purpose of this paper.

After the estimation of the residual height the DEM of the scene is updated, the compensation for the topographic height can now be performed correctly and the geocoding locations are corrected as well.

2.3. Single change detector

Coherent change detection methods exploit also the phase information typical of any coherent acquisition system being in this way sensible to small variation of the geometric structure of the scene. Several methods have been exploited in the past using multi-temporal and/or multi-polarimetric SAR data (Akbari et al., 2016; Barber, 2015; Jung et al., 2018).

A review of the algorithm presented in (Monti-Guarnieri et al., 2018) is fundamental to introduce the novelty provided by this contribution in the next section.

The time series of a pixel in a SAR image can be seen as a realization of a zero mean, complex multivariate normal process with probability density function (PDF)

$$f(\mathbf{x}) = \frac{exp\left(-\mathbf{x}^H \mathbf{C}^{-1} \mathbf{x}\right)}{\pi^{N_i} |\mathbf{C}|} \tag{6}$$

where $\mathbf{C}$ is the covariance matrix, N_i the number of images in the stack and $|\cdot|$ the determinant operator.

The algorithm proposed is based on the Generalized Likelihood Ratio Test (GLRT) which involves the comparison between two PDFs.

The covariance matrix can be modeled in two ways (for the sake of clarity we assume to have just 4 images in the stack):

1. A matrix $\mathbf{C}_0$ representing a stable target is composed as follows

$$\mathbf{C}_0 = \sigma_p^2 \begin{bmatrix} 1 & \gamma_p & \gamma_p & \gamma_p \\ \gamma_p & 1 & \gamma_p & \gamma_p \\ \gamma_p & \gamma_p & 1 & \gamma_p \\ \gamma_p & \gamma_p & \gamma_p & 1 \end{bmatrix} = \sigma_p^2 \Gamma_0 \tag{7}$$

where Γ_0 is the so-called coherence matrix and σ_p is the backscattered

power and γ_p is the interferometric coherence.

2. A matrix $\mathbf{C}_{N_c}$ representing a target that decorrelates after the image N_c is composed as follows (we suppose again 4 images and the decorrelation happening after image $N_c = 2$)

$$\mathbf{C}_0 = \sigma_p^2 \begin{bmatrix} 1 & \gamma_p & 0 & 0 \\ \gamma_p & 1 & 0 & 0 \\ 0 & 0 & 1 & \gamma_p \\ 0 & 0 & \gamma_p & 1 \end{bmatrix} = \sigma_p^2 \Gamma_{N_c} \tag{8}$$

In the two models just presented a further assumption has been made: the backscattered power doesn't change between one image and the other. The final detector can be formulated as:

$$Z(\mathbf{x}) = log\left(\frac{f(\mathbf{x}|\mathbf{C}_0)}{f(\mathbf{x}|\mathbf{C}_{N_c})}\right) = N_s log\left(\frac{|\Gamma_{N_c}|}{|\Gamma_\mathbf{0}|}\right) - N_s Tr\left(\left(\Gamma_0^{-1} - \Gamma_{N_c}^{-1}\right)\widehat{\Gamma_x}\right) \underset{H_0}{\overset{H_1}{\lessgtr}} \Lambda \tag{9}$$

where N_s is the number of independent samples used to estimate the coherence matrix $\widehat{\Gamma_\mathbf{x}}$ and Λ is a threshold for the detection.

All the possible Γ_{N_c} are tested against $\Gamma_\mathbf{0}$ and when $Z(\mathbf{x})$ happens to be under a certain threshold a detection is triggered.

This kind of processing is suitable when we want to reach high resolution and we need high sensibility to small changes. For the detection of big changes such as construction and destruction works, a simple incoherent analysis (on a couple of images or a time series) can be sufficient: this kind of processing is more cost effective in term of computational load, but the final accuracy is reduced due to the missed exploitation of the phase information provided by any coherent acquisition system.

CCD, moreover, maintains a large number of degrees of freedom in the sense that several parameters may be tuned resulting in completely different outputs: the threshold, the polarization, the estimation window, the number of images used and their temporal sampling are all independent parameters that must be tuned.

The presented method was designed for the detection of a single change in the stack. The single change model is the most appropriate in the case of a stable area that is affected by a sudden decorrelation (see (Monti-Guarnieri et al., 2018)), but this is not the case in urban environments. In fact, in such an evolving domain multiple decorrelations are frequent.

2.4. Extended CCD for multiple changes: M-CCD

In case of an unknown number of changes, the statistically optimal detector becomes quite rapidly unfeasible since we have to test all the possible coherence matrices with all the possible number of changes (i.e. all the matrices with one, two, up to $N_i - 1$ changes): this is computationally unfeasible since the total number of test to perform is in the order of $2^{N_i-1} - 1$.

Two sub-optimal detectors (from now on called M-CCDs) can be formulated with a significantly lower computational load:

1. Local minima M-CCD: supposing only one change in the covariance matrix it's possible to find all the local minima under a certain threshold in the GLRT history: this solution is computationally inexpensive since the number of covariance matrices to be tested is just $N_i - 1$.
2. Segmentation-based M-CCD: supposing again only one change in the covariance matrix the algorithm proceeds by finding the absolute minimum of the GLRT history. If it's over threshold the procedure ends with no detections, while if it's under threshold the dataset is segmented and the GLRT repeated in the two subsets now generated. The procedure continues in a recursive manner until no more absolute minima are detected under threshold. This method is computationally more intensive than the first one.

In Fig. 3 an artificial example is shown where a dataset is generated with 20 images and with 2 change points at images 10 and 17 respectively and with a very high coherence level $\gamma_p = 0.8$. In this specific case both local minima and segmentation approach can correctly detect the two change points.

In particular, in Fig. 3a the coherence matrix of the simulated scenario is depicted.

In Fig. 3b two local minima of the likelihood function are found under threshold and they correspond exactly to the change points in the stack.

In Fig. 3c, d, e the segmentation approach is depicted: in this case the absolute minimum is found at image 10 and, since it is under threshold, a detection is triggered and the dataset is segmented. In Fig. 3d the first subset is tested and no points are found under threshold. In Fig. 3e the second subset is tested and here a change is found under threshold.

In this specific case, both approaches reach the correct result. The single change detector, instead, would have identified only the biggest change in the stack (the absolute minimum of the GLRT function).

To compare the performances of the two procedures, a Monte-Carlo simulation has been executed. The setup of the simulation consists of a synthetic dataset of 30 images showing 3 changes at different time instants: one at the beginning of the dataset and two very close to each other in the middle. The number of samples used to estimate the covariance matrix is 3: such a small sample size is used to simulate the real scenario where we want to obtain the highest resolution possible and where the estimate of the sample coherence matrix has a large variance superimposed. In the framework of multi-change detector, there is not a unique way to define what is a correct detection and what is a false alarm since a detector may trigger a change in a correct position, but at the same time miss the others: the detection is correct, but it's not complete. In our scenario we decided to be as severe as possible, so, when we simulate a dataset with multiple change points, if the detector triggers all the detection in the correct positions we call that a "correct detection" while if it detects just a portion of changes it's not counted as correct detection. On the other end, a false alarm event is triggered even if only one change is detected in a synthetic dataset with no changes.

From Fig. 4b it's evident that the probability of false alarm is exactly the same for the two detectors. This is expected and it is due to the fact that the absolute minimum is always also a local minimum, thus, the number of false detections is the same. For high values of coherence, the curve converges to zero.

The difference is in the probability of correct detection (Fig. 4a): the segmentation based approach is more reliable and it reaches good probability of correct detection even for relatvively low coherences where instead the local minima procedure is not detecting accurately enough. The reason is clarified in Fig. 3: a change in the middle of the time series generates an accentuated notch in the likelihood function, shadowing a possible change at the end (or at the beginning) of the dataset that would hardly be detected.

On the other end, segmenting the stack is equivalent to eliminate the biggest change by taking only a portion of the coherence matrix increasing in this way the probability of triggering a detection in the correct position. For the following, we decided to keep only the second solution since it's the one showing better performances, while keeping at the same time the computational processing quite low.

From now on, every time we will refer to M-CCD, it is implied that we use the segmentation-based M-CCD just explained.

In Fig. 4 we used just 3 looks to estimate the coherence matrix to obtain and high resolution estimate of the changes. It is important to remember that the samples used should be statistically homogeneous, otherwise the performances of the estimator are degraded.

Statistical homogeneity in the space domain can be generally guaranteed by performing a similarity test between pixels such as the Kolgomorov Smirnov test (Ferretti et al., 2011). Such tests, however, are mainly based on the amplitude time series of a target. For the changes

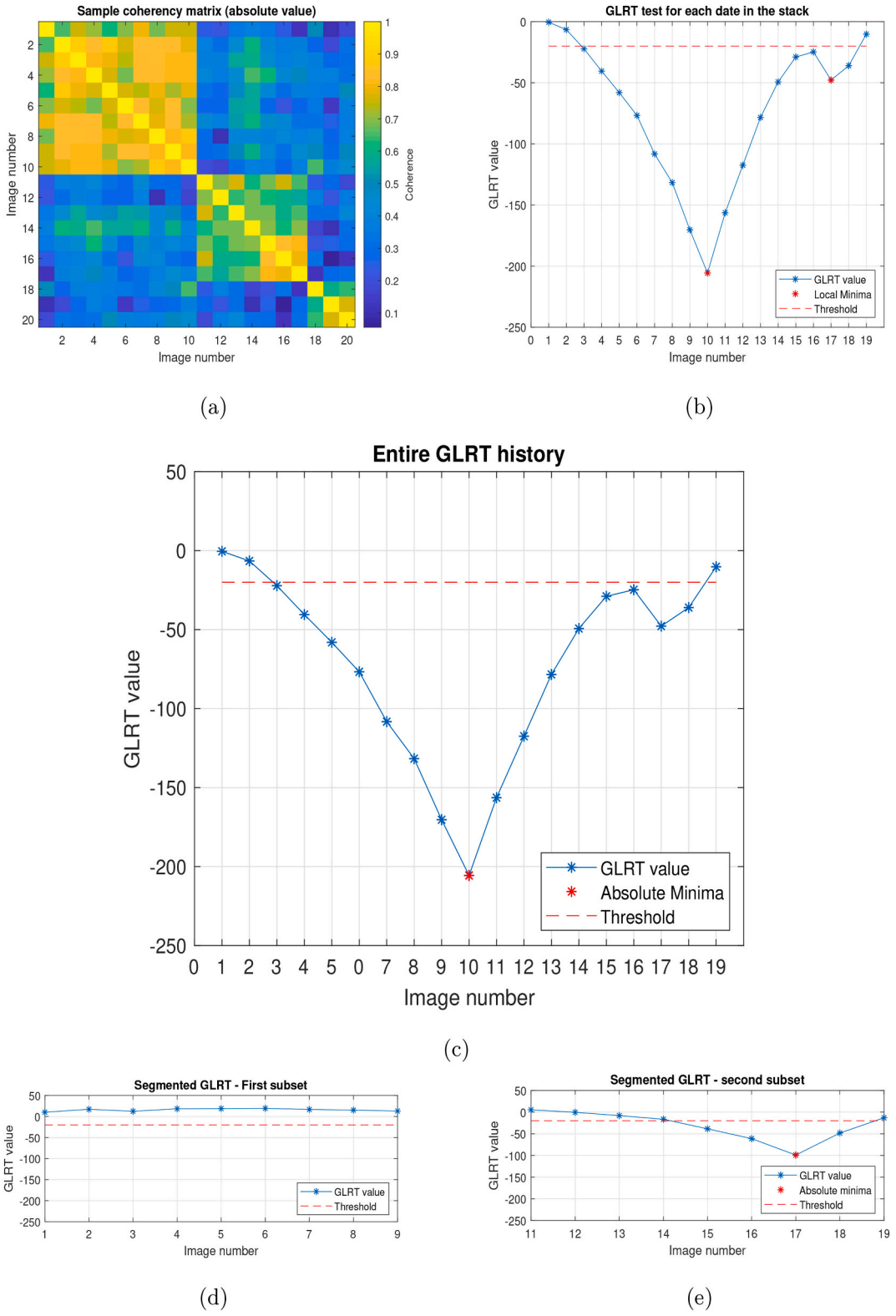

Fig. 3. (a) Coherence matrix with 20 images and two changes. (b) The likelihood function: two detection are triggered by the local minima approach since both local minima are under the threshold. (c) The absolute minimum is under threshold, so the segmentation approach triggers a detection. (d) The first subset from image 1 to 10 is tested and no changes are found. (e) In the second subset from image 11 to 20 a change is found.

that are of interest for this processing, an amplitude-based test may not be effective since the amplitude itself may not vary after the decorrelation time instant.

If two polarizations are used together to estimate a single coherence matrix (doubling in this way the number of looks) homogeneity must not only be searched in the space domain but also in the polarization domain. Usually two polarizations can see different objects: the assumption behind the usage of both at the same time is that we are searching for decorrelation of the signal that is in turn tightly related to the geometric structure of the target on ground. When the complex

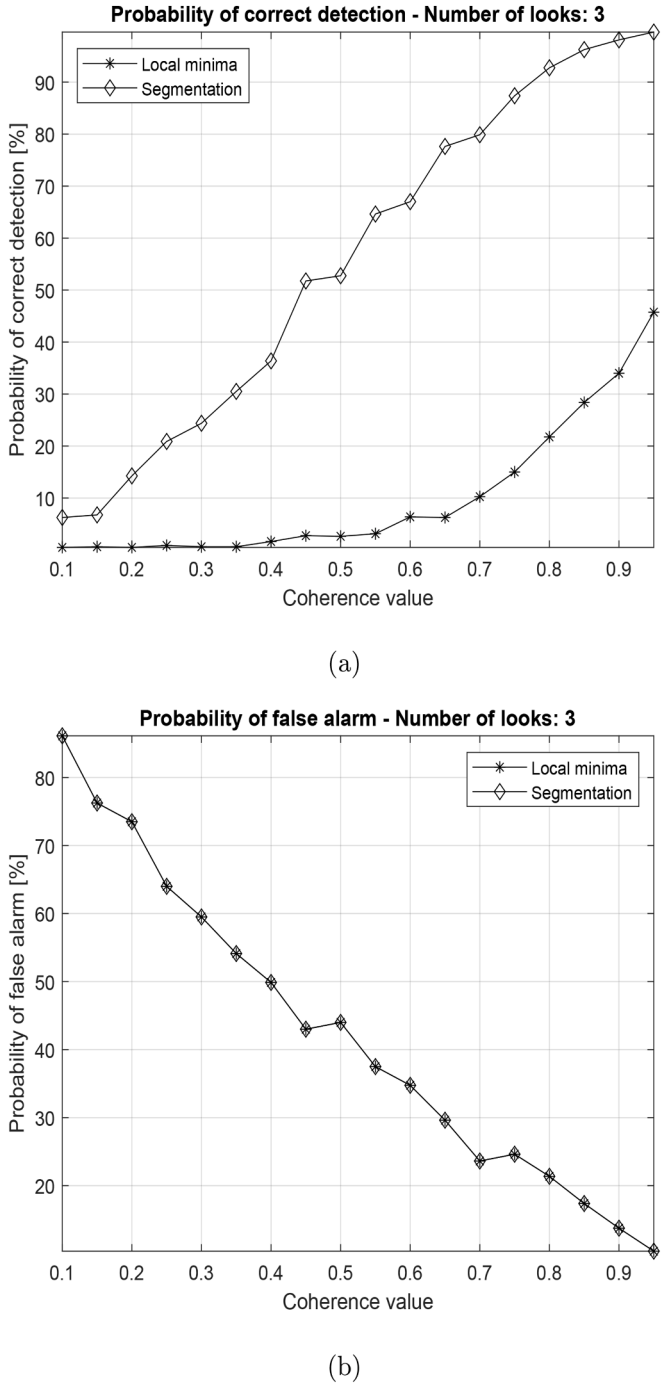

Fig. 4. (a) Probability of correct detection for the two sub-optimal algorithms. The M-CCD segmentation approach shows significantly better performances than the local minima approach. (b) False alarm rate for the two techniques. The probability of false alarm is the same for the two methods since an absolute minima is always also a local minima.

reflectivity changes (suddenly decorrelates) we assume it does so in both polarization having in this way statistical homogeneity between the two. If this hypothesis is not verified in practice, we are in presence of a Non-Homogeneous Pixel (NHP) in the set of pixels used to estimate the coherence matrix. In the following we will refer to NHP without specifying if the dishomogeneity happen in the space or polarization domain.

In Fig. 5a Monte-Carlo simulation with a varying number of NHP has been made. The number of NHP inside the estimation window is limited from 1 to 4: if, for example, the VV polarization sees the decorrelation

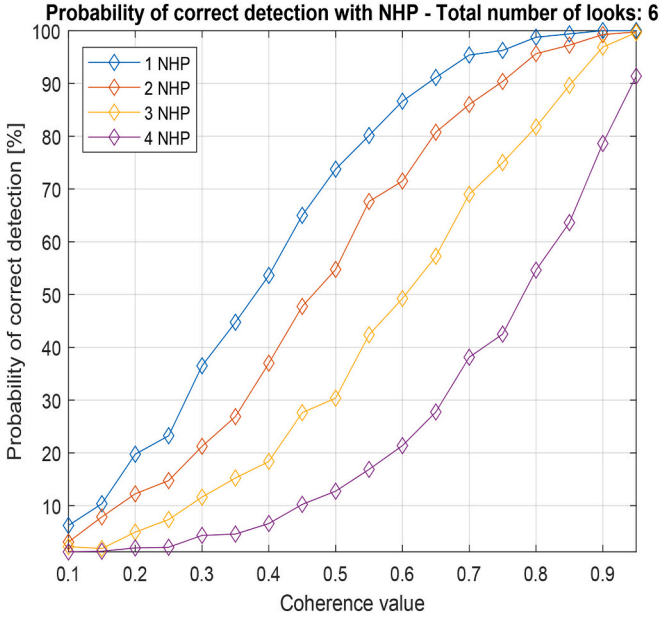

Fig. 5. Probability of correct detection for the M-CCD in presence of Non Homogeneous Pixel (NHP). The total number of looks is 6 in order to comply with the small number of looks in the case study (3) and dual-pol data (VV and VH).

while the VH does not, the number of NHP is 3 out of 6 total looks in the window.

Another interesting aspect is the threshold for the detection hereinafter denoted by Λ. It's important to notice that Λ depends on N_s, the true coherences between each interferometric couple, the total temporal size of the stack, and the position of the supposed change inside the dataset. For this reason, a threshold able to guarantee a Constant False Alarm Rate (CFAR) is not trivial at all to find (Mian et al., 2018).

The authors found that a good rule of thumb is to take a threshold that is doubled with respect to N_s. It's useful to remark, also, that N_s is a conveniently small number: using a lot of samples in the space domain, in fact, would improve the quality of the estimate of $\widehat{\Gamma_x}$ at the expense of worsening the resolution. Using a stack of N_i images instead of just two allows the trading between space and time reaching in this way a very high resolution (at the expense of a higher computational burden).

The final output of the CCD processing is a set of geolocated points, each one representing a triggered detection in a particular location and in a particular time instant.

In order to further reduce the number of false alarms and to identify buildings affected by changes, a post-processing of such points is mandatory as explained in detail in the following section.

2.5. GIS post-processing

This procedure aims to process the detections obtained by the M-CCD in order to identify and extract only the buildings interested by changes. In order to do so, it is necessary to exploit a geospatial dataset related to land use/land cover. The availability of such datasets is ensured almost everywhere thanks to the diffusion of open data policies or crowd-sourced mapping initiatives such as OpenStreetMap (Jokar Arsanjani et al., 2015).

It is worth remembering that the objective of this processing is not to classify or interpret the changes, but to simply identify them by excluding all the detection happening on non built-up areas such as parks, parking lots, water bodies and so on. The post-processing is a two-step GIS-based procedure. Since the change detection dataset refers to any generic change, the first step is a selection by location which allows the extraction of the subset of points specifically located inside the buildings polygons, thus the subset of points (or targets, in radar jargon)

that identifies changes over buildings.

The second and final step focuses on the identification of the buildings interested by changes (hereinafter SAR-detected buildings) and it is performed by associating to each building polygon the total number of points lying inside it. Obviously, the greater the number of points characterizing a building, the more significant the changes occurred.

3. Case study

3.1. Dataset description

In this section, a validation of the entire procedure is carried out over the city of Manchester, UK (Fig. 6).

In this example we used a set of 17 SAR images gathered by the constellation Sentinel-1 from June 2015 to December 2016. The description of the case study is summarized in Table 1.

Table 1
Description of the case study.

Parameter	Value
City	Manchester (UK)
Area size	$120km^2$
Total number of buildings	62,331
Platform	Sentinel-1 A/B
Number of images used	17
Acquisition start	June 2015
Acquisition end	November 2016

3.2. M-CCD results

The CCD processing has several degrees of freedom: first of all the spatial window where the coherence matrix is estimated can be changed arbitrarily. A small window reaches higher resolution, but, the elements of the coherence matrix have high bias and variance superimposed (Touzi et al., 1999).

The choice of the threshold is also tightly related to the number of independent looks taken for the estimation of the coherence matrix as it is clear from eq. 9.

The polarization can be taken as VV only, VH only or VV + VH in the sense that both are averaged for the coherence matrix estimation. While different polarization can sense different aspects of the target on ground and therefore different behavior along time (Cloude and Papathanassiou, 1998), in this paper we assumed that a decorrelation happens simultaneously in the VV and VH polarization. If this assumption turns out to be true for a specific target we have doubled the number of looks used for the estimation of the coherence matrix, while if it turns out to be false we can relate to the case where there are statistically non-homogeneous pixels in the estimation window.

In the following we have tested different combinations of parameters: each combination is hereinafter called RUN. Each RUN with the corresponding set of parameters is depicted in Table 2.

The first three runs have a very small spatial window obtaining thus higher spatial resolution. The difference between the three is either the polarization used, the threshold or the estimation of the residual height. Note that, if one single polarization is used, the threshold is reduced accordingly to take into account the reduced number of looks. The last run has a much bigger spatial window (and a very stringent threshold) loosing resolution but gaining in estimation accuracy of the coherence matrix. A 31×5 pixels window corresponds roughly to an area on ground of $75m \times 75m$: an even bigger window can be used, but statistical homogeneity can't be guaranteed in such an heterogeneous environments as the urban one.

Table 2
Configuration for each RUN tested for the case study of Manchester.

RUN	Window size	Resolution	Pol	Threshold (Λ)	Estimated residual height
RUN01	[5,1]	12×10	VV + VH	-20	false
RUN02	[5,1]	12×10	VV	-12	true
RUN03	[5,1]	12×10	VV + VH	-20	true
RUN04	[5,1]	75×70	VV + VH	-150	true

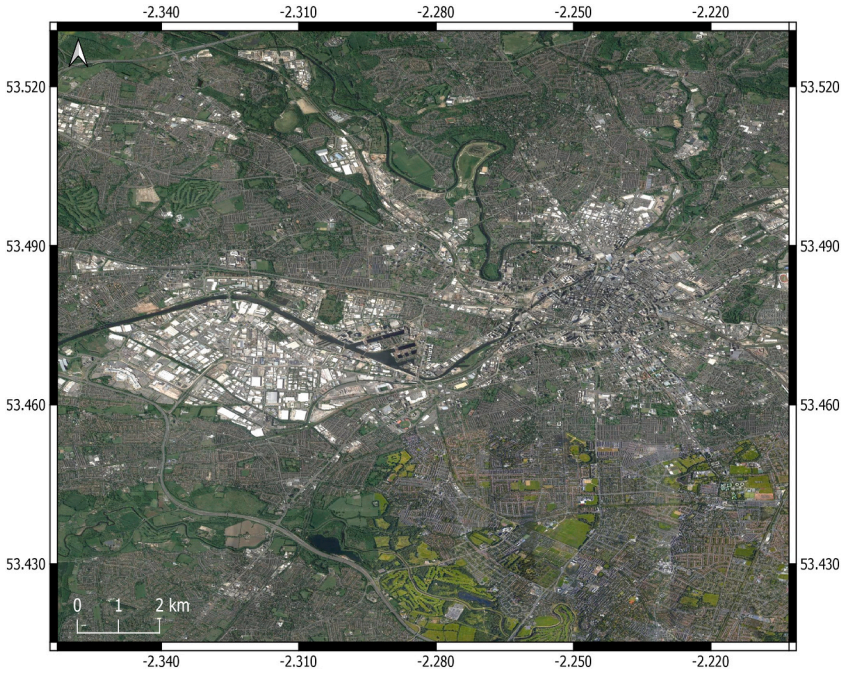

Fig. 6. Manchester, UK; extent of the region of interest provided in WGS84 reference system (Map data: @2019 Google).

3.3. GIS post-processing

The GIS post-processing was performed by exploiting the vector dataset of buildings of Manchester related to the year 2015, which is provided as open data by the national mapping agency for Great Britain (Ordnance Survey).

Table 3 reports information about the detections resulting from each RUN.

RUN02 obtains the largest amount of total changes (more than 240,000) while RUN03 obtains the smallest amount of total changes (about 14,000). It is worth noticing that the selection of the subset of changes located inside buildings allows for a significant reduction of the total number of identified changes: the initial detections are reduced by percentages which range between 66% and 84%. This means that a huge amount of changes that are not located on buildings are discarded by the first step of the GIS procedure.

The extraction of the SAR-detected buildings (i.e. the buildings with at least one change) was performed by taking into account the whole time period of SAR imagery, i.e. from June 2015 to November 2016.

As mentioned in Subsection 2.5, for each RUN, a vector dataset of buildings with the corresponding number of detected changes was generated.

Table 3 also shows that the RUN02 identifies the largest amount of buildings with at least one change (11,313). RUN03, although characterized by a total number of changes lower than RUN04, identifies a number of SAR-detected buildings doubled (1675), meaning that there are many buildings with associated a very low number of changes.

In RUN01 and RUN03 the threshold has been kept the same on purpose to evaluate the effects of the residual height estimation on the number of detections. In RUN02, on the other end, a much less aggressive threshold is used and the number of detections increases accordingly.

Notice how the extraction the SAR-detected buildings decreases by a significant amount the total number of changes in the scene highlighting those changes happening over man-made structures.

A more detailed analysis of results can be performed by taking into account the number of changes associated with each building. Fig. 7 shows an example of SAR-detected buildings dataset derived from RUN01 on a limited area of Manchester. Buildings are classified according to the number of changes that characterize them: it is clear that most of the buildings are affected by a number of changes lower or equal to 5 (blue colored buildings).

Fig. 8 shows, for each RUN, how the number of SAR-detected buildings varies according to different thresholds χ representing the minimum number of changes per building needed to classify a building as "changed".

As expected, the graph highlight that the more the threshold χ increases the more the number of changed buildings decreases. In particular, a steep drop in SAR-detected buildings number is showed for χ values ranging between 1 and 5: considering χ equal to 3, the number of SAR-detected buildings is reduced of 50% for RUN04 and of 70% for the other RUNS; if χ is set to 5, the SAR-detected buildings are reduced by 60% for RUN04 and by 85% for the other RUNS. This behavior points out the importance of the threshold parameter χ, which needs to be accurately calibrated.

Table 3
Results obtained from each RUN: number of total changes detected by the extended CCD method, number of changes only related to buildings, and number of buildings interested by at least one change.

RUN	Total changes	Changes over buildings	Buildings
RUN01	61,181	14,844	4154
RUN02	243,491	40,141	11,313
RUN03	14,545	4973	1675
RUN04	33,188	7818	724

The operation of thresholding will discard some building that are changed (even one change is still a change after all), but it will also highlights those buildings that are much more affected by homogeneous and spatially extended decorrelation. When the threshold χ increases, the number of SAR-detected buildings for each RUN converge meaning that the choice of the configuration of the estimator is less and less important. If a lot of changes are inside the boundaries of a building, they will be detected no matter the size of the estimation window, the polarization or the selected detection threshold (Λ).

To compare the degree of overlapping between the different RUNs with varying thresholds we used the Matthews Correlation Coefficient (MCC) defined as

$$MCC = \frac{TP \times TN - FP \times FN}{\sqrt{(TP + FP)(TP + FN)(TN + FP)(TN + FN)}} \tag{10}$$

where *TP* stands for True Positive, *TN* for True Negative, *FP* for False Positive and *FN* for False Negative. The MCC is able to represent with a single number the confusion matrix: for a MCC equal to 1 there is perfect accordance between the two methods, while for MCC equal to -1 there is perfect dis-accordance.

The MCC has been computed by considering thresholds on the number of changes per building equal to 1,5,10 and 20. The results are depicted in Table 4a–d respectively.

It is easy to see that when the threshold increases, all the coefficients increase. This means that the detections of the different RUNs with high thresholds are overlapping. In particular, the last column of each table is quite interesting: it represents the comparison between the first three high-resolution RUNs with the only low-resolution one. When χ increases we are discarding a lot of changed building and therefore we are making the high-resolution RUN working as the low-resolution one. When χ is lower, instead, there are a lot of changed building that are not detected by RUN04 making the MCC significantly lower.

3.4. Comparison with high-resolution optical images

Since no ground truth is available over the city of Manchester, we must rely on high resolution optical images for the interpretation of the changes. Due to the high cloud cover of northern UK, few images were usable and the ones that shown the highest resolution possible were available through the Google Earth Pro®database.

While low resolution images like Sentinel-2, RapidEye and PlanetScope are more regularly spaced in time, their spatial resolution or quality (due to cloud coverage or bad illumination conditions) is not sufficient for a visual interpretation. In Section 4, however, we will use RapiEye images for an automatic detection of changes to assess the performances of low-res optical images. Google Earth images, on the other end, are very coarsely spaced in time, but their resolution goes down to less than 50 cm allowing for a better visual interpretation.

Since thousand of changed buildings have been detected, a random sample of buildings of significant size was extracted for each RUN by using the formula:

$$S = \frac{a}{1 + a/N} \tag{11}$$

where

$$a = \frac{z^2 p(1-p)}{e^2} \tag{12}$$

where S is the sample size to be taken, N is the total number of buildings, z is the pre-computed $z - score$ derived from the desired confidence level (in this case equal to 95%), e is the desired margin of error (5%) and p the probability of changed building (set to the maximum level of uncertainty of 50%).

For each sample's building, the verification of changes on the optical images was performed. It is worth noting that no threshold value χ was

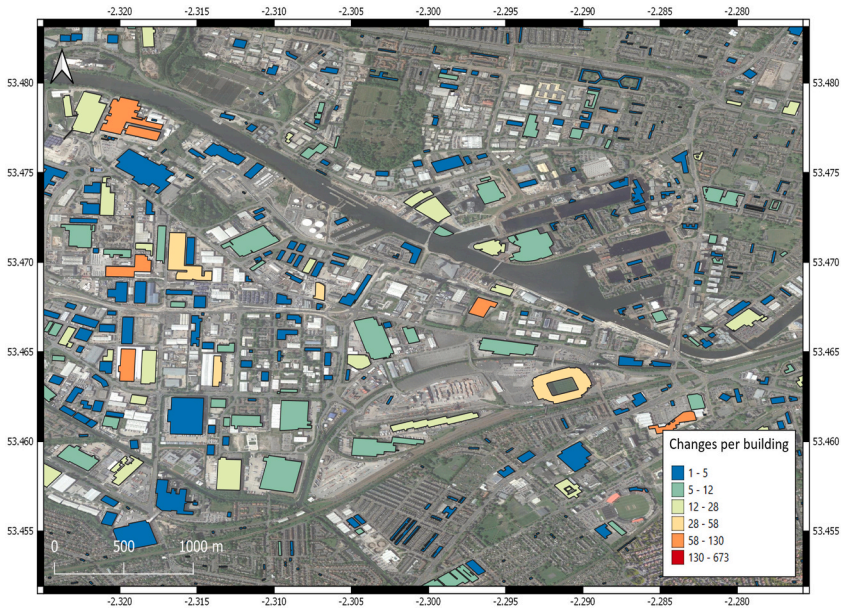

Fig. 7. Classification of buildings according to the number of changes. Zoom of the results achieved by the joint SAR-GIS method over a limited area of Manchester (Map data: @2019 Google; Ordnance Survey data ©Crown copyright and database right 2013).

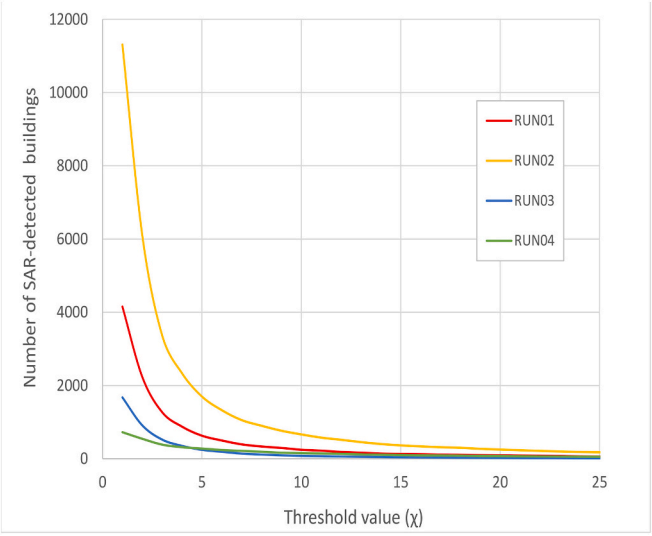

Fig. 8. Number of changed buildings based on different threshold values χ.

imposed, thus all the buildings with at least one change were taken into account. Results of comparison, proposed in Fig. 9, show that for all the considered RUNS about 60% of SAR-detected changes are also visible in optical images (blue color bar). Besides the identification of new buildings or destroyed buildings, the SAR method proved to be able to detect also minor changes such as roofing replacements (Fig. 10a) or installation of photo-voltaic panels (Fig. 10b).

For what concerns the disagreements, i.e. the SAR-detected changes to buildings not confirmed by optical, several different reasons can be adduced as an explanation. From the optical side, some changes can be missed due to different illumination conditions between the images. From the SAR side, there are many conditions that can cause the non-confirmed change detections. During the comparison activity, three different kinds of conditions were considered:

1. The existence of parkings at the top of the buildings or adjacent to them (Fig. 10c);
2. The presence of trees covering part of the buildings (Fig. 10d);
3. The existence of construction sites, and thus storage areas for materials and vehicles, nearby the buildings (Fig. 10e).

Table 4
Matthews correlation coefficients (MCC) between RUNs (01,02,03,04) computed for different thresholds χ.

(a) $\chi = 1$

	01	02	03	04
01	1	0.44	0.52	0.22
02		1	0.28	0.15
03			1	0.20
04				1

(b) $\chi = 5$

	01	02	03	04
01	1	0.55	0.61	0.40
02		1	0.38	0.30
03			1	0.32
04				1

(c) $\chi = 10$

	01	02	03	04
01	1	0.59	0.58	0.51
02		1	0.38	0.39
03			1	0.38
04				1

(d) $\chi = 20$

	01	02	03	04
01	1	0.57	0.56	0.62
02		1	0.36	0.49
03			1	0.41
04				1

According to the comparison analysis proposed in Fig. 9, parking areas (red color bar) could be responsible for most of the non-confirmed detections (22%–26%). Trees (green color bar) could generally affect a low percentage of the non-confirmed detections (3.5%–5%) with exception for RUN02, where the percentage increases to 8%. The construction sites (yellow color bar) were identified nearby the 3%–4.5% of

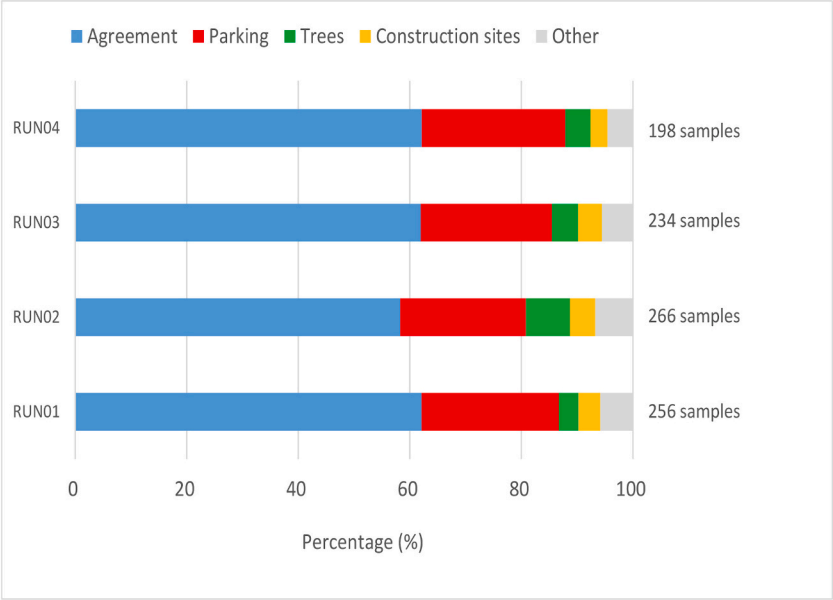

Fig. 9. Validation of SAR-detected changes per building by photo interpretation of optical imagery. The percentage of agreement, i.e. the SAR-detected changes confirmed by optical, is about 60% (blue color) for all the RUNS. Disagreements are due to the presence of parking, 22% - 26% (red color), trees, 3.5% - 8% (green color), and construction sites, 3% - 4.5% (yellow color), nearby the SAR-detected buildings. The percentage of buildings in gray color (4.5% - 7%) represents the added value provided by SAR with respect to optical. (For interpretation of the references to color in this figure legend, the reader is referred to the web version of this article.)

the SAR-detected buildings. Unlike the previous two cases, although they are not directly referred to the evaluated building, they still confirm a situation of urban change. Finally, the remaining percentage values, which range between 4.5% - 7% (gray color bar), refers to SAR detections not confirmed by optical for which no specific explanation was found; thus, they can be considered the added value provided by SAR with respect to optical.

4. Comparison with other change detection techniques

In this section we want to compare the proposed technique with other optical and SAR change detection methods.

For what concerns SAR, we processed the same dataset with the Omnibus detector described in (Nielsen et al., 2016) and with the visualization tool REACTIV (Rapid and EAsy Change detection on Time-series using the coefficient of Variation).

Given N_i images ($N_i \geq 2$) the Omnibus detector tests if the polarimetric covariance matrices are all equal or not through a likelihood ratio test in which

$$H_0: \quad \Sigma_0 = \Sigma_1 = \ldots = \Sigma_{N_i}$$
$$H_1: \quad \text{otherwise}$$

where Σ_i is the polarimetric covariance matrix for the i^{th} observation. For the estimation of the polarimetric covariance matrix we used the same spatial window as in the M-CCD in order to have a fair comparison between the two methods.

The REACTIV detector uses instead the temporal coefficient of variation (standard deviation $\times$ mean^{-1}) described in (Ferretti et al., 2001) to assess the temporal variability of the scatterers on ground. REACTIV simply encodes the coefficient of variation as the saturation in the HSV color space. The result is a map where colored and brilliant pixels are affected by a change, while desaturated pixels are the stable ones. For both Omnibus and REACTIV a detection with a suitable threshold has been used to produce a binary map where a pixel is marked as changed/not changed.

In Fig. 11a small subset of the city of Manchester is represented where changes detected by Omnibus (Fig. 11a) and REACTIV (Fig. 11b) are highlighted in red.

In the optical domain, instead, we used two RapidEye images with 5 m of resolution acquired with a temporal baseline of less than one year (10th of June 2015 the first one, the 9th of May 2016 the second one).

After a pre-processing consisting in atmospheric correction and histogram equalization, the two images are compared by performing a Principal Component Analysis (PCA as in (Bustos et al., 2011)). From now on this method will be simply called OPCA (Optical PCA). A threshold is now imposed on the score values of the PCA to produce a binary map of changes. In Fig. 12 an example of detection is depicted.

In order to perform a fair comparison we binarized also M-CCD RUNs: a pixel is set to true if there is at least on change in the time series, false otherwise. The threshold χ now only represents a lower limit for the spatial extent of the change.

To compare the different RUNs with all the different methods we used again the MCC described in Section 3.3.

In Table 5 we can notice that when the threshold increases the degree of accordance also increases. When the threshold is small, the high resolution and high sensitivity M-CCD detects a huge amount of changed buildings that are not detected by the other methods due to the poor sensibility (radiometric SAR analysis) or poor resolution (optical): the MCC is thus quite low.

When we increase the threshold we are discarding all those buildings affected by a small number of changes. The remaining ones are buildings that are severely affected by decorrelations that are usually visible also with optical imagery. Moreover, a change that involves a wide area usually has a strong radiometric signature (i.e. destruction, renovations, etc.) making easier for incoherent methods the detection: that's why the MCC increases with the threshold.

While the MCC improves, it still remains quite small: this is attributable to the deep difference between the working principles of the different detectors analyzed. The M-CCD is a coherent high resolution method, Omnibus and REACTIV are incoherent high resolution method and the OPCA rely of low resolution images gathered by an independent sensor. These results highlight the importance of the threshold χ: making it bigger intrinsically lower down the resolution of the M-CCD processor making it more similar to the optical one. While it is possible to highlight changes involving a wide area starting from very high resolution change map, it is impossible to do the inverse. Starting from a low resolution image it is impossible to obtain a map of changes at high resolution.

5. Conclusions

This paper proposes a technique aimed at estimating changes in an urban scenario in a fast, robust and reliable way.

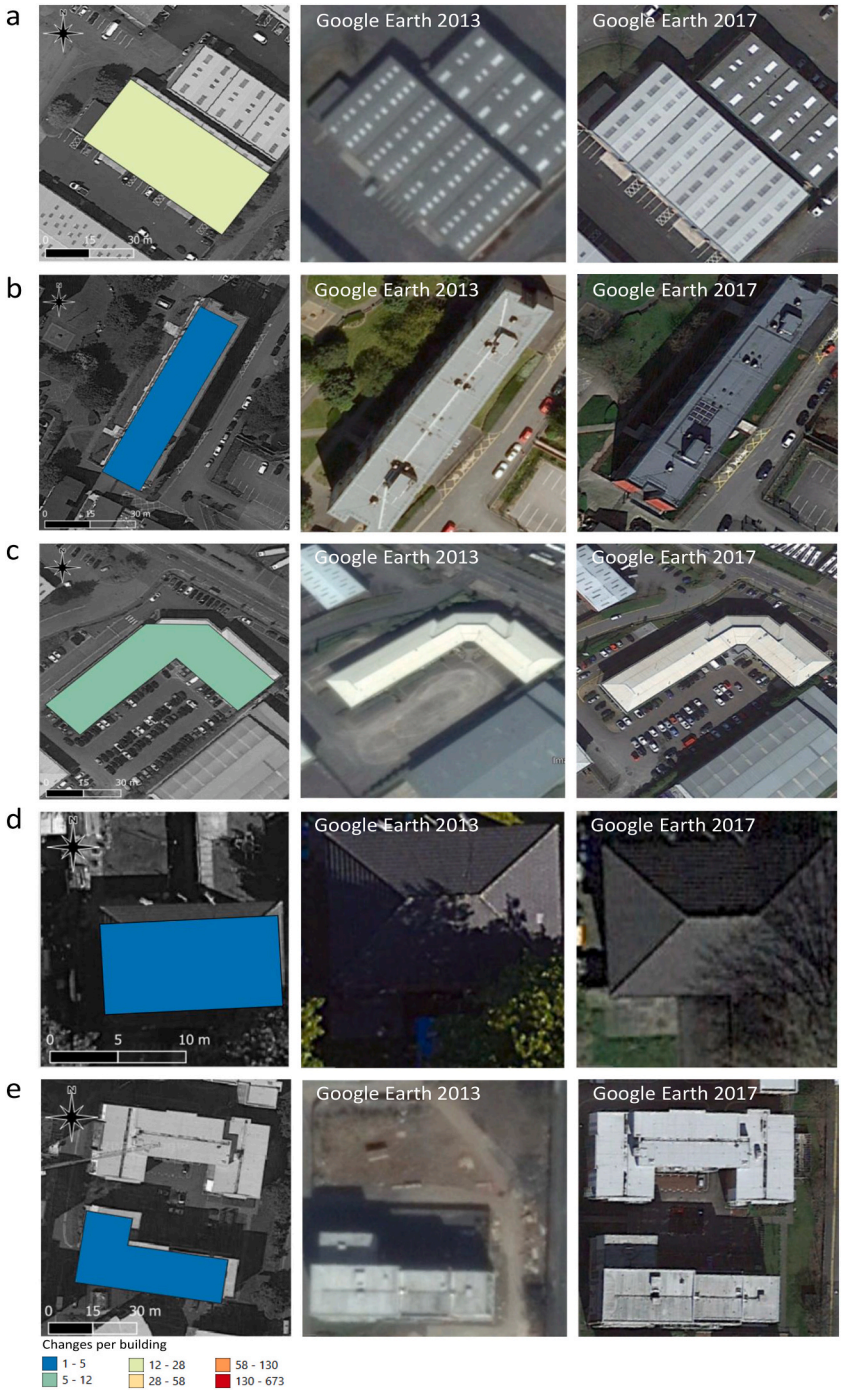

Fig. 10. SAR-optical comparison: example of SAR confirmed detections due to roofing replacements (a) and photovoltaic installation (b); example of non-confirmed detections probably due to the presence of parking areas (c), trees (d), and construction sites (e) nearby the building of interest. For each example the number of changes per building (Map data: @2019 Google; Ordnance Survey data ©Crown copyright and database right 2013) and the optical images related to the years 2013 and 2017 (Map data: Google, Maxar Technologies) are proposed.

The main challenge of any coherent change detector in an urban scenario is to discard a huge number of unwanted detections both in space and time. The former is due to subtle and uninteresting changes in the geometric structure of a target while the latter is due to the temporal instability shown by the urban environment when long time series are used.

To overcome this drawback we have set up a simple workflow composed by a pre-processing routine, an extended CCD and a GIS-based post-processing. A case study has been performed over the city of Manchester (UK) where different M-CCD configurations have been tested. The GIS post-processing confirmed its capability to significantly reduce the detections identified by extended CCD method by removing 60% - 80% of the total changes. Furthermore, by increasing the threshold on the number of detection falling inside the polygon representing a building (χ), we are able to highlight major changes that are detected by all the RUNs.

A manual comparison has been done with high-resolution optical images over the same area: a good agreement (about 60%) is presented between the two datasets and, in most of the cases where there is no agreement (28% - 31%), the cause of the divergence can be attributed to nearby parking lots or forested areas that fell inside the estimation window and that are able to trigger unwanted detections.

Finally, a comparison with other techniques from both the SAR and optical world has been carried out. The accordance between the methods improves, as expected, with higher thresholds on the number of change detected per-building.

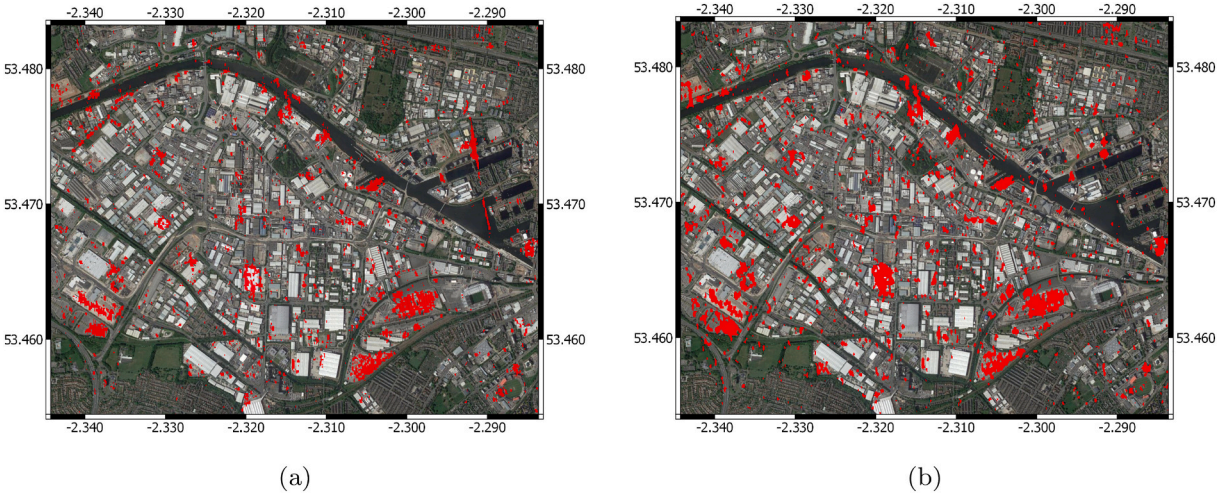

Fig. 11. Changes detected by Omnibus (a) and REACTIV (b) over a small subset of the city of Manchester. The two detectors use the same dataset of the M-CCD detector described in Table 1.

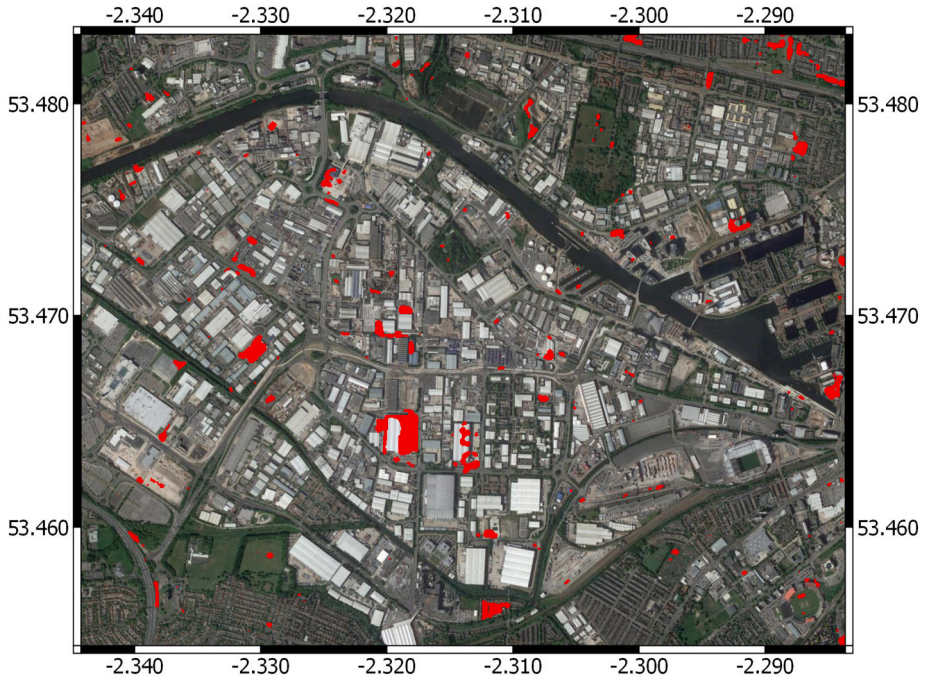

Fig. 12. Changes detected by the exploitation of two RapidEye optical images and a PCA analysis on the difference between the two. The nominal resolution of the images is 5 m.

The M-CCD is an high-resolution and high sensitivity method able to detects every subtle geometric change. By selecting a higher threshold we discard all the changes not involving a wide area, making the result more similar to the low resolution methods. It is important to notice that the sensibility is not changed after the thresholding, therefore we are still able to detect subtle changes conditioned to the fact that they involve a wide area (e.g. solar panel installation).

The proposed processing chain is able to adaptively satisfy the user needs: if high resolution is required, then no threshold is applied and the full set of changes over buildings can be assessed. If instead it is important to highlight areas with wide changes, a simple thresholding is sufficient to discard a lot of unwanted detection. It is useful to notice that this is impossible by exploiting medium resolution optical images or SAR-based incoherent methods: in the former small changes can't be detected due to the poor resolution while in the latter the sensibility will be poor with respect to the coherent method.

Credit author statement

Marco Manzoni: Conceptualization, Data curation, Formal analysis, Methodology, Software, Validation, Writing - original draft, Writing - review and editing

Andrea Virgilio Monti Guarnieri: Conceptualization, Formal analysis, Methodology

Monia Elisa Molinari: Conceptualization, Data curation, Formal analysis, Methodology, Software, Validation, Writing - original draft, Writing - review and editing

Table 5
Matthews correlation coefficient (MCC) between RUNs (01,02,03,04) and the Omnibus, REACTIV and OPCA. Here the threshold χ refers only to the spatial extent of the change.

(a) $\chi = 1$			
	OMNIBUS	REACTIV	OPCA
RUN01	0.21	0.15	0.08
RUN02	0.18	0.14	0.07
RUN03	0.21	0.15	0.08
RUN04	0.14	0.10	0.07
(b) $\chi = 5$			
	OMNIBUS	REACTIV	OPCA
RUN01	0.26	0.24	0.16
RUN02	0.26	0.27	0.19
RUN03	0.23	0.21	0.15
RUN04	0.15	0.17	0.13
(c) $\chi = 10$			
	OMNIBUS	REACTIV	OPCA
RUN01	0.28	0.23	0.20
RUN02	0.28	0.24	0.22
RUN03	0.22	0.16	0.16
RUN04	0.2	0.22	0.15
(d) $\chi = 20$			
	OMNIBUS	REACTIV	OPCA
RUN01	0.22	0.23	0.22
RUN02	0.28	0.23	0.24
RUN03	0.15	0.14	0.15
RUN04	0.15	0.21	0.19

Declaration of Competing Interest

The authors declare that they have no known competing financial interests or personal relationships that could have appeared to influence the work reported in this paper.

References

Aiazzi, B., Alparone, L., Baronti, S., Garzelli, A., Zoppetti, C., 2013. Nonparametric Change Detection in Multitemporal SAR Images Based on Mean-Shift Clustering. IEEE Trans. Geosci. Remote Sens. 51, 2022–2031. URL: http://ieeexplore.ieee.org/document/6479281/ https://doi.org/10.1109/TGRS.2013.2238946.

Akbari, V., Anfinsen, S.N., Doulgeris, A.P., Eltoft, T., Moser, G., Serpico, S.B., 2016. Polarimetric SAR change detection with the complex hotelling–lawley trace statistic. IEEE Trans. Geosci. Remote Sens. 54, 3953–3966. https://doi.org/10.1109/TGRS.2016.2532320 (Conference Name: IEEE Transactions on Geoscience and Remote Sensing).

Atwood, D.K., Thirion-Lefevre, L., 2018. Polarimetric phase and implications for urban classification. IEEE Trans. Geosci. Remote Sens. 56, 1278–1289. https://doi.org/10.1109/TGRS.2017.2750211 (Conference Name: IEEE Transactions on Geoscience and Remote Sensing).

Barber, J., 2015. A generalized likelihood ratio test for coherent change detection in polarimetric SAR. IEEE Geosci. Remote Sens. Lett. 12, 1873–1877. https://doi.org/10.1109/LGRS.2015.2433134 (conference Name: IEEE Geoscience and Remote Sensing Letters).

Biondi, F., 2018. (L + S)-RT-CCD for Terrain Paths Monitoring. IEEE Geosci. Remote Sens. Lett. 15, 1209–1213. URL: https://ieeexplore.ieee.org/document/8357816/ https://doi.org/10.1109/LGRS.2018.2830644.

Bovolo, F., Bruzzone, L., 2005. A detail-preserving scale-driven approach to change detection in multitemporal SAR images. IEEE Trans. Geosci. Remote Sens. 43, 2963–2972. URL: http://ieeexplore.ieee.org/document/1542367/ https://doi.org/10.1109/TGRS.2005.857987.

Bovolo, F., Marin, C., Bruzzone, L., 2013. A Hierarchical Approach to Change Detection in Very High Resolution SAR Images for Surveillance Applications. IEEE Trans. Geosci. Remote Sens. 51, 2042–2054. URL: http://ieeexplore.ieee.org/document/6392252/ https://doi.org/10.1109/TGRS.2012.2223219.

Bujor, F., Trouve, E., Valet, L., Nicolas, J.M., Rudant, J.P., 2004. Application of log-cumulants to the detection of spatiotemporal discontinuities in multitemporal SAR images. IEEE Trans. Geosci. Remote Sens. 42, 2073–2084. URL: http://ieeexplore.ieee.org/document/1344160/ https://doi.org/10.1109/TGRS.2004.835304.

Bustos, C., Campanella, O., Kpalma, K., Magnago, F., Ronsin, J., 2011. A method for change detection with multi-temporal satellite images based on principal component analysis. In: 2011 6th International Workshop on the Analysis of Multi-Temporal Remote Sensing Images (Multi-Temp), pp. 197–200. https://doi.org/10.1109/Multi-Temp.2011.6005082.

Chini, M., Pelich, R., Hostache, R., Matgen, P., Lopez-Martinez, C., 2018. Towards a 20 m Global Building Map from Sentinel-1 SAR Data. Remote Sens. 10, 1833. URL: https://www.mdpi.com/2072-4292/10/11/1833 https://doi.org/10.3390/rs10111833 (number: 11 Publisher: Multidisciplinary Digital Publishing Institute).

Cloude, S., Papathanassiou, K., 1998. Polarimetric SAR interferometry. IEEE Trans. Geosci. Remote Sens. 36, 1551–1565. https://doi.org/10.1109/36.718859 (Conference Name: IEEE Transactions on Geoscience and Remote Sensing).

Colin Koeniguer, E., Nicolas, J.M., 2020. Change Detection Based on the Coefficient of Variation in SAR Time-Series of Urban Areas. Remote Sens. 12, 2089. URL: https://www.mdpi.com/2072-4292/12/13/2089 https://doi.org/10.3390/rs12132089 (number: 13 Publisher: Multidisciplinary Digital Publishing Institute).

De Zan, F., Monti Guarnieri, A., 2006. TOPSAR: Terrain Observation by Progressive Scans. IEEE Trans. Geosci. Remote Sens. 44, 2352–2360. URL: http://ieeexplore.ieee.org/document/1677745/ https://doi.org/10.1109/TGRS.2006.873853.

Ehrlich, D., Melchiorri, M., Florczyk, A.J., Pesaresi, M., Kemper, T., Corbane, C., Freire, S., Schiavina, M., Siragusa, A., 2018. Remote Sensing Derived Built-Up Area and Population Density to Quantify Global Exposure to Five Natural Hazards over Time. Remote Sens. 10, 1378. URL: https://www.mdpi.com/2072-4292/10/9/1378 https://doi.org/10.3390/rs10091378 (number: 9 Publisher: Multidisciplinary Digital Publishing Institute).

Ferretti, A., Prati, C., Rocca, F., 2001. Permanent Scatterers in SAR interferometry. IEEE Trans. Geosci. Remote Sens. 39, 13.

Ferretti, A., Fumagalli, A., Novali, F., Prati, C., Rocca, F., Rucci, A., 2011. A New Algorithm for Processing Interferometric Data-Stacks: Squee SAR. IEEE Trans. Geosci. Remote Sens. 49, 3460–3470. URL: http://ieeexplore.ieee.org/document/5765671/ https://doi.org/10.1109/TGRS.2011.2124465.

Freeman, A., 1992. SAR calibration: an overview. IEEE Trans. Geosci. Remote Sens. 30, 1107–1121. https://doi.org/10.1109/36.193786 (Conference Name: IEEE Transactions on Geoscience and Remote Sensing).

Gamba, P., Tupin, F., Weng, Q., 2008. Introduction to the issue on remote sensing of human settlements: status and challenges. IEEE J. Select. Top. Appl. Earth Observ. Remote Sens. 1, 82–86. https://doi.org/10.1109/JSTARS.2008.2004250.

Hakdaoui, S., Emran, A., Pradhan, B., Lee, C.W., Nguemhe Fils, S.C., 2019. A Collaborative Change Detection Approach on Multi-Sensor Spatial Imagery for Desert Wetland Monitoring after a Flash Flood in Southern Morocco. Remote Sens. 11, 1042. URL: https://www.mdpi.com/2072-4292/11/9/1042 https://doi.org/10.3390/rs11091042 (number: 9 Publisher: Multidisciplinary Digital Publishing Institute).

Hanssen, R., 2001. Radar Interferometry Data Interpretation and Error Analysis, p. 2. https://doi.org/10.1007/0-306-47633-9.

OpenStreetMap in GIScience. In: Jokar Arsanjani, J., Zipf, A., Mooney, P., Helbich, M. (Eds.), 2015. Lecture Notes in Geoinformation and Cartography. Springer International Publishing, Cham. https://doi.org/10.1007/978-3-319-14280-7. URL:

Jung, J., Kim, D.J., Lavalle, M., Yun, S.H., 2016. Coherent change detection using InSAR temporal decorrelation model: a case study for volcanic ash detection. IEEE Trans. Geosci. Remote Sens. 54, 5765–5775. https://doi.org/10.1109/TGRS.2016.2572166 (Conference Name: IEEE Transactions on Geoscience and Remote Sensing).

Jung, J., Yun, S.H., Kim, D.J., Lavalle, M., 2018. Damage-mapping algorithm based on coherence model using multitemporal polarimetric–interferometric SAR data. IEEE Trans. Geosci. Remote Sens. 56, 1520–1532. https://doi.org/10.1109/TGRS.2017.2764748 (Conference Name: IEEE Transactions on Geoscience and Remote Sensing).

Luo, B., Hu, C., Su, X., Wang, Y., 2019. Differentially Deep Subspace Representation for Unsupervised Change Detection of SAR Images. Remote Sens. 11, 2740. URL: https://www.mdpi.com/2072-4292/11/23/2740 https://doi.org/10.3390/rs11232740 (number: 23 Publisher: Multidisciplinary Digital Publishing Institute).

Manzoni, M., Monti-Guarnieri, A.V., Realini, E., Venuti, G., 2020. Joint Exploitation of SAR and GNSS for Atmospheric Phase Screens Retrieval Aimed at Numerical Weather Prediction Model Ingestion. Remote Sens. 12, 654. URL: https://www.mdpi.com/2072-4292/12/4/654 https://doi.org/10.3390/rs12040654.

Marin, C., Bovolo, F., Bruzzone, L., 2015. Building Change Detection in Multitemporal Very High Resolution SAR Images. IEEE Trans. Geosci. Remote Sens. 53, 2664–2682. URL: http://ieeexplore.ieee.org/document/6948368/ https://doi.org/10.1109/TGRS.2014.2363548.

Melchiorri, M., Florczyk, A.J., Freire, S., Schiavina, M., Pesaresi, M., Kemper, T., 2018. Unveiling 25 Years of Planetary Urbanization with Remote Sensing: Perspectives from the Global Human Settlement Layer. Remote Sens. 10, 768. URL: https://www.mdpi.com/2072-4292/10/5/768 https://doi.org/10.3390/rs10050768 (number: 5 Publisher: Multidisciplinary Digital Publishing Institute).

Mian, A., Ovarlez, J.P., Ginolhac, G., Atto, A.M., 2018. A Robust Change Detector for Highly Heterogeneous Multivariate Images. In: 2018 IEEE International Conference on Acoustics, Speech and Signal Processing (ICASSP). IEEE, Calgary, AB, pp. 3429–3433. URL: https://ieeexplore.ieee.org/document/8462253/ https://doi.org/10.1109/ICASSP.2018.8462253.

Mian, A., Ginolhac, G., Ovarlez, J.P., Atto, A.M., 2019. New Robust Statistics for Change Detection in Time Series of Multivariate SAR Images. IEEE Trans. Signal Process. 67, 520–534. URL: https://ieeexplore.ieee.org/document/8552453/ https://doi.org/10.1109/TSP.2018.2883011.

Monti-Guarnieri, A.V., Brovelli, M.A., Manzoni, M., Mariotti d'Alessandro, M., Molinari, M.E., Oxoli, D., 2018. Coherent Change Detection for Multipass SAR. IEEE Trans. Geosci. Remote Sens. 56, 6811–6822. URL: https://ieeexplore.ieee.org/document/8401705/ https://doi.org/10.1109/TGRS.2018.2843560.

Montuori, A., Luzi, G., Bignami, C., Gaudiosi, I., Stramondo, S., Crosetto, M., Buongiorno, M.F., 2016. The interferometric use of radar sensors for the urban

monitoring of structural vibrations and surface displacements. IEEE J. Select. Top. Appl. Earth Observ. Remote Sens. 9, 3761–3776. https://doi.org/10.1109/JSTARS.2016.2571324 (Conference name: IEEE journal of selected topics in applied earth observations and remote sensing).

Moreira, A., Prats-Iraola, P., Younis, M., Krieger, G., Hajnsek, I., Papathanassiou, K.P., 2013. A tutorial on synthetic aperture radar. IEEE Geosci. Remote Sens. Magaz. 1, 6–43. URL: http://ieeexplore.ieee.org/document/6504845/ https://doi.org/10.1109/MGRS.2013.2248301.

Nielsen, A.A., Conradsen, K., Skriver, H., 2016. Omnibus test for change detection in a time sequence of polarimetric SAR data. In: 2016 IEEE International Geoscience and Remote Sensing Symposium (IGARSS), pp. 3398–3401. https://doi.org/10.1109/IGARSS.2016.7729878 (iSSN: 2153-7003).

Novak, L.M., 2005. Change detection for multi-polarization multi-pass SAR. In: Algorithms for Synthetic Aperture Radar Imagery XII. International Society for Optics and Photonics, pp. 234–246. URL: https://www.spiedigitallibrary.org/conference-proceedings-of-spie/5808/0000/Change-detection-for-multi-polarization-multi-pass-SAR/10.1117/12.609894.short https://doi.org/10.1117/12.609894.

Olen, S., Bookhagen, B., 2018. Mapping Damage-Affected Areas after Natural Hazard Events Using Sentinel-1 Coherence Time Series. Remote Sens. 10, 1272. URL: https://www.mdpi.com/2072-4292/10/8/1272 https://doi.org/10.3390/rs10081272 (number: 8 Publisher: Multidisciplinary Digital Publishing Institute).

Pan, Z., Hu, Y., Wang, G., 2019. Detection of short-term urban land use changes by combining SAR time series images and spectral angle mapping. Front. Earth Sci. 13, 495–509. URL: https://doi.org/10.1007/s11707-018-0744-6.

Perissin, D., Wang, T., 2011. Time-series InSAR applications over urban areas in China. IEEE J. Select. Top. Appl. Earth Observ. Remote Sens. 4, 92–100. https://doi.org/10.1109/JSTARS.2010.2046883.

Rignot, E., van Zyl, J., 1993. Change detection techniques for ERS-1 SAR data. IEEE Trans. Geosci. Remote Sens. 31, 896–906. URL: http://ieeexplore.ieee.org/document/239913/ https://doi.org/10.1109/36.239913.

Sansosti, E., Berardino, P., Manunta, M., Serafino, F., Fornaro, G., 2006. Geometrical SAR image registration. IEEE Trans. Geosci. Remote Sens. 44, 2861–2870. URL: http://ieeexplore.ieee.org/document/1704979/ https://doi.org/10.1109/TGRS.2006.875787.

Tamura, M., 2015. Mapping urban damage of the 2011 East-Japan earthquake using multi-temporal PALSAR images. In: 2015 IEEE International Geoscience and Remote Sensing Symposium (IGARSS), pp. 3576–3578. https://doi.org/10.1109/IGARSS.2015.7326594 (iSSN: 2153-7003).

Touzi, R., Lopes, A., Bruniquel, J., Vachon, P., 1999. Coherence estimation for SAR imagery. IEEE Trans. Geosci. Remote Sens. 37, 135–149. URL: http://ieeexplore.ieee.org/document/739146/ https://doi.org/10.1109/36.739146.

Wahl, D.E., Yocky, D.A., Jakowatz, C.V., Simonson, K.M., 2016. A New Maximum-Likelihood Change Estimator for Two-Pass SAR Coherent Change Detection. IEEE Trans. Geosci. Remote Sens. 54, 2460–2469. URL: https://ieeexplore.ieee.org/document/7378311/ https://doi.org/10.1109/TGRS.2015.2502219.

Washaya, P., Balz, T., Mohamadi, B., 2018. Coherence Change-Detection with Sentinel-1 for Natural and Anthropogenic Disaster Monitoring in Urban Areas. Remote Sens. 10, 1026. URL: https://www.mdpi.com/2072-4292/10/7/1026 https://doi.org/10.3390/rs10071026 (number: 7 Publisher: Multidisciplinary Digital Publishing Institute).